Polymer 50 (2009) 4656–4670

Contents lists available at ScienceDirect

Polymer

journal homepage: www.elsevier.com/locate/polymer

Poly(3-hydroxybutyrate-*co*-3-hydroxyhexanoate) nanocomposites with optimal mechanical properties

Yuping Xie [a], Doug Kohls [b], Isao Noda [c], Dale W. Schaefer [b], Yvonne A. Akpalu [b,d,*]

[a] Department of Chemical and Biological Engineering, Rensselaer Polytechnic Institute, Troy, NY 12180, USA
[b] Department of Chemical and Materials Engineering, University of Cincinnati, Cincinnati, OH 45221, USA
[c] The Procter & Gamble Company, Beckett Ridge Technical Center, 8611 Beckett Road, West Chester, OH 45069, USA
[d] Department of Chemistry and Chemical Biology, Rensselaer Polytechnic Institute, Troy, NY 12180, USA

ARTICLE INFO

Article history:
Received 24 March 2009
Received in revised form
30 June 2009
Accepted 4 July 2009
Available online 21 July 2009

Keywords:
Bioplastics
Renewable polymer
Nanocomposite

ABSTRACT

With the ultimate goal to design renewable polymer nanocomposites with optimal mechanical properties, this study reports an investigation of structure–property relationships for a model system – silica/poly(3-hydroxybutyrate-*co*-3-hydroxyhexanoate) (PHBHx) nanocomposites. Two molecular weights of PHBHx ($M_w = 903{,}000$ g/mol and $M_w = 633{,}000$ g/mol) and two types of silica nanoparticles (nominally spheres and fibers according to the manufacturer) were used to prepare the nanocomposites. Small-angle X-ray scattering shows that the sphere and fiber nanoparticles had similar surface areas and primary particle size, but differed in degree of aggregation of the primary particles. The thermal stability of the PHBHx matrix was slightly improved by the addition of nanofillers. Simultaneous improvement of both stiffness and toughness was observed at 1-wt% loading for the higher molecular weight matrix. The more highly aggregated SiO_2 fibers had a greater toughening effect than the SiO_2 spheres. Compared to the unfilled polymer matrix, a 30% increase in Young's modulus and 34% increase in toughness were obtained for the 1-wt% SiO_2 fiber/PHBHx072 nanocomposite. The addition of SiO_2 spheres to PHBHx072 resulted in the same increase in Young's modulus (30%) but a smaller increase (11%) in toughness. The dramatic increases in modulus for PHBHx072 cannot be explained on the basis of two-component micromechanical models. Apparently the filler alters the character of the semicrystalline matrix. When the loading was 3 wt% and above, Young's modulus continued to increase, but the strain at break and toughness decreased. The ultimate strength did not change compared with the unfilled polymer. In order to understand the mechanical properties observed, the thermal behavior, spherulitic morphology and the deformation mechanisms of the nanocomposites and the dispersion state of the nanofillers were studied. We found that a high molecular weight of the polymer matrix, weak interfacial adhesion and a good dispersion of the nanofillers are necessary to improve toughness and stiffness simultaneously.

1. Introduction

The progressive dwindling of fossil resources, coupled with increasing public preference for environmentally friendly plastics, has increased academic and industrial interests in biodegradable polymers prepared from renewable sources [1]. Polyhydroxyalkanoates (PHAs) are biodegradable and thermoplastic polyesters produced by a variety of bacteria from renewable resources like corn sugar and oil. In comparison with petroleum-based plastics, PHAs need less energy for production [2], can reduce the green house gas emissions [2] and generate less landfill waste. PHAs can replace petroleum-based amorphous and semicrystalline polymers currently in use for packaging, adhesives, and coating applications.

PHAs have recently attracted considerable interest because of their biodegradability and biocompatibility [3–14]. Since PHAs are produced from renewable resources and biodegrade to carbon dioxide and water, they are often described as environmentally friendly plastics [15].

PHAs also offer significant advantages in medical applications, particularly in tissue engineering [6,16,17]. Recent studies [18,19] have shown that poly(3-hydroxybutyrate-*co*-3-hydroxyhexanoate) (PHBHx) tissue scaffolds have better mechanical properties and biocompatibility than other biodegradable polymers, such as polylactic acid (PLA). In addition, the use of PHAs in biodegradable personal hygiene articles, such as diapers, has already been described [8].

* Corresponding author. Department of Chemical and Materials Engineering, University of Cincinnati, 110 8th Street, Cincinnati, OH 45221, USA. Tel.: +1 518 894 4489; fax: +1 513 556 2569.
E-mail address: yvonne.akpalu@uc.edu (Y.A. Akpalu).

0032-3861/$ – see front matter © 2009 Elsevier Ltd. All rights reserved.
doi:10.1016/j.polymer.2009.07.023

The homopolymer poly(3-hydroxybutyrate) (PHB) and the copolymer poly(3-hydroxybutyrate-*co*-3-hydroxyvalerate) (PHBV) are the best-known types of PHAs. However, brittle behavior caused by high crystallinity, poor thermal stability, and narrow processing windows limit the application of these PHAs [9,12]. To improve the overall physical properties of PHB, PHAs containing over 125 types of monomers have been harvested from different microorganisms [20]. The copolymers show a wide range of physical properties depending on the chemical structure of the comonomer units as well as the comonomer composition.

PHA copolymers comprising 3-hydroxybutyrate units and a relatively small amount of other medium-chain-length 3-hydroxyalkanoate (mcl-3HA) comonomers with side groups of at least three carbon units provide a set of useful properties, including polyolefin-like thermo-mechanical properties and polyester-like physicochemical properties, not achieved by PHB or PHBV. The incorporation of mcl-3HA units effectively lowers the crystallinity and melting temperature (T_m). The T_m of mcl-3HA copolymers of PHA can be lowered well below the thermal decomposition temperature of PHB and PHBV to make this material much easier to process. The reduced crystallinity of mcl-3HA copolymers of PHA provides the ductility and toughness required for many practical applications [9]. Although the copolymerization improves toughness, however, it decreases stiffness. Thus it is imperative to find alternative ways to improve stiffness and strength without sacrificing toughness so that the mechanical properties of PHAs match or exceed those of petroleum-based polymers.

For polymers, the goal is often a material with high toughness and a large plastic strain at break, while retaining other desirable properties, such as stiffness and strength. These are opposite demands. The usual technique – rubber toughening – has the disadvantage of a pronounced decrease in strength and stiffness due to the rubber content [21].

Addition of small amounts of nanofillers (<5 wt%) such as nanoclays to form nanocomposites is a means to improve multiple properties [22–24], such as mechanical, barrier, electrical and thermal properties, especially when good dispersion is achieved [25–29]. Adding nanofillers usually makes the polymer more brittle, while increasing the stiffness and tensile strength. For example, He et al. [30] found that for clay/polyamide-6 nanocomposites Young's modulus and yield strength increased but the strain at break decreased with increasing clay content. Hassan et al. [11] studied the mechanical properties of clay/PHBHx nanocomposites and found substantial improvement in Young's moduli, but at the cost of decreased strain at break and toughness. Recently, several studies of PHA nanocomposites have been reported [10,11,31–40] but no information exists on PHBHx nanocomposites with improved thermal properties, stiffness and toughness.

While thermal properties [9,12,14,41–43], mechanical properties [9,15,44–46], environmental benefits [2,4], and enzymatic degradation [15,46–50] of pure mcl-3HA copolymers of PHAs have been studied in detail over the last 10 years, a systematic study of the influence of the nanoparticle structure on the mechanical properties has not been reported. In this article we report the successful preparation of silica/PHBHx nanocomposites. Improved mechanical and thermal properties are correlated with filler morphology determined by electron microscopy, polarized optical microscopy and small-angle X-ray scattering.

2. Experimental

2.1. Materials

The copolymers of poly(3-hydroxybutyrate-*co*-3-hydroxyhexanoate) (PHBHx) of $M_w = 903{,}000$ g/mol with 7.2 mol% hydroxyhexanoate (HHx) content (PHBHx072) and $M_w = 633{,}000$ g/mol and $M_n = 333{,}000$ g/mol with 6.9 mol% HHx content (PHBHx069) were provided by The Procter & Gamble Co. The characteristics of the polymers are shown in Table 1. The polymers were purified before use. The purification process was described in detail earlier [12].

Table 1
Weight average molecular weight (M_w), number average molecular weight (M_n), and the short chain branch content (SCB, the mole content of HHx) of the polymers used.

Polymer	M_w (g/mol)	M_n (g/mol)	SCB (mol%)
PHBHx072	903,000	–	7.2
PHBHx069	633,000	333,000	6.9

The SiO_2 nanoparticles were obtained from Nissan Chemical America Corporation. According to Nissan, the spheres have a nominal diameter of 10–15 nm, and the SiO_2 fibers have a diameter of 9–15 nm and a length of 40–100 nm. More precise characterization is reported below. The particles were used without further processing. The characteristics of these nanofillers are listed in Table 2.

2.2. Nanocomposite preparation

The nanocomposites with different filler loadings (1.0, 3.0 and 5.0 wt%) were processed by a "fast evacuation" method reported earlier [51,52]. The copolymers were diluted by chloroform to a 1-wt% solution. The pre-calculated nanoparticle solution was diluted by the addition of chloroform, sonicated by the VCX-750 ultrasonic processor (Sonics & Materials, Inc.) for two minutes, and added to the 1-wt% polymer solution. The resulting solution was sonicated for two more minutes and poured into Petri dishes, and then dried in a vacuum oven at room temperature for two days.

The effect of sonication on the mechanical properties of neat PHBHx069 was studied (data not shown). Sonication of the neat polymer solution for two minutes did not influence Young's modulus, ultimate strength and strain at break, indicating that molecular weight and polydispersity of the polymer were not altered, which is consistent with Bansal's previous work [53,54]. In this study, unsonicated neat polymers were used to prepare the control samples.

2.3. Characterization

2.3.1. Differential scanning calorimetry (DSC)

DSC was performed with a DSC Q100 (TA Instruments). The sample was heated from room temperature to 180 °C and soaked for five minutes, followed by cooling to −80 °C at 1 °C/min. The reported melting temperature (T_m) was determined from the second heating from −80 °C to 190 °C at a rate of 10 °C/min. DSC experiments were performed under nitrogen (flow rate of 50 mL/min) using 5–15 mg samples. The crystallinity was calculated using the equation of $X_c = \Delta H_f/[(1-\Phi)\Delta H^0]$, where Φ is the weight fraction of the nanofiller, ΔH^0 is the heat of fusion for perfect PHBHx crystals (115 J/g) [12], and ΔH_f is the measured heat of fusion for PHBHx.

Table 2
Properties of the silica nanoparticles used in this study (Courtesy of Nissan Chemical America Corporation).

Label	Organosilicasol™	Particle Size (nm)	Surface area[a] (m^2/g)	Aspect ratio[a] (L/D)
SiO_2	IPA-ST (spheres)	10–15	200–300	1
SiO_2 fiber	IPA-ST-UP (fibers)	9–15/40–100[b]	140–250	3–11

[a] Surface area and aspect ratio were calculated based on Nissan nominal values of L and D.
[b] Elongated particles have a diameter (D) of 9–15 nm with a length (L) of 40–100 nm.

2.3.2. Thermogravimetric analysis (TGA)

TGA was done with a TGA Q50 (TA Instruments) to determine the mass loss as a function of temperature. The thermal stability was also studied by TGA. Samples were heated from 30 °C to 900 °C at a rate of 20 °C/min under a 50 mL/min dry N_2 flow. Sample sizes of 10–15 mg were used. To obtain accurate filler loadings, we subtracted the background of the empty crucible heated under the same conditions.

2.3.3. Polarized optical microscopy (POM)

POM measurements were performed on film samples sealed between two round glass cover slips at room temperature. An optical microscope (Olympus BX51) coupled to an Insight digital camera was used to characterize the solid-state morphology of film samples (~15 μm thick). Before any measurements were taken, samples were first melted at 180 °C for five minutes under nitrogen to remove any thermal history, and then cooled to room temperature at 1 °C/min. All the melting and cooling procedures were performed on a computer-interfaced Instec HCS600V hot stage to minimize sample movement and temperature fluctuations.

2.3.4. Field emission scanning electron microscope (FESEM)

The fracture surfaces of specimens after the tensile tests were coated with platinum to prevent charging and studied with a JEOL JSM-6335 FESEM. A filament emission current of 10–12 μA was accelerated towards the sample with a voltage of 5 kV.

2.3.5. Ultra-small-angle X-ray scattering (USAXS)

USAXS measurements were carried out at the X-ray Operations and Research beamline 32-ID-B, located at the Advanced Photon Source (APS), Argonne National Laboratory (Argonne, IL, USA). At this beamline, a Bonse–Hart camera allows one to record USAXS scattering curves in a q range from 0.0001 to 1.0 $Å^{-1}$. The scattering vector q is the independent variable in small-angle scattering and is related to the scattering angle (θ), via the relation $q = (4\pi/\lambda)\sin(\theta/2)$, where λ is the X-ray wavelength. After subtraction of an air background, the USAXS data were desmeared using routines provided by APS.

The samples had disk-like shapes with diameters of 6.5 mm and thicknesses of approximately 1 mm. The samples were heated to 170 °C in three minutes and stabilized at 170 °C for five minutes before the measurements were taken. The samples were kept at 170 °C while being measured to assure that the polymer crystallites were melted.

2.3.6. Tensile testing

Samples for tensile tests were prepared by compression molding to Type-V dimensions in ASTM D 638-02. To obtain the sample thickness of about 0.30 mm, 0.2 g of each sample was used. The samples were heated in a dog-bone mold at 180 °C under pressure of one metric ton for ten minutes and then slowly cooled to room temperature with the heater off while still under pressure. The cooling process took about three hours, so the cooling rate was about 1 °C/min.

The mechanical properties were measured using tensile tests in accordance with ASTM 882-02 (for thin films less than 1.0 mm in thickness) at room temperature on an Instron (Model 5843) load frame with a 1-kN load cell and an Instron video-extensometer. The speed of testing was 1 mm/min. Young's modulus was determined from the slope in the elastic region (0–0.4% strain) of the stress–strain curve. The toughness was calculated by taking the area under the stress–strain curve. The ultimate strength was obtained from the maximum stress on the stress–strain curve. At least five replicates were tested to obtain an average value. All samples were tested after two days of conditioning at 23 ± 2 °C and 50 ± 5% relative humidity (RH).

The effect of sample thickness (0.3 mm vs. 1.0 mm) on the mechanical properties of neat PHBHx was studied (data not shown). Thicker samples showed a slight increase in Young's modulus, ultimate strength and strain at break. The thinner samples (0.3 mm) were used in this study.

3. Data analysis

3.1. USAXS data analysis

The USAXS data were analyzed in several ways. The most generic approach is fitting to unified model proposed by Beaucage et al. [55–57]. The unified method is useful to ascertain the size scales associated with various levels of hierarchical structures such as aggregates and agglomerates [58]. The unified method assumes a series of structural levels consisting of a Guinier-like region followed by a power-law or Porod region:

$$I(q) = \sum_{i=1}^{n}\left(G_i\exp\left(-q^2R_{g_i}^2/3\right) + B_i\exp\left(-q^2R_{g_{i+1}}^2/3\right) \times\left\{\left[\operatorname{erf}\left(qkR_{g_i}/6^{1/2}\right)\right]^3/q\right\}^{P_i}\right) \quad (1)$$

Here $i = 1$ refers to the smallest-size structural level. G_i is the Guinier pre-factor; B_i is the power-law pre-factor; R_{g_i} is the average radius of gyration; and P_i the power-law of the structural level i respectively. We used 2-level fits ($n = 2$), in which case level 1 refers the elementary building blocks or primary particles and level-2 describes how these elementary particles are aggregated. In some cases we used three levels ($n = 3$). Level 3 was added to account for excess scattering at very small q, which is due to scattering from bubbles or imperfections on the surface of the sample. The Irena 2.32 package [59] was used to fit the scattering data.

For a sphere of radius r, the radius of gyration R_g is obtained [60,61] by

$$R_g = \sqrt{\frac{3}{5}}r \quad (2)$$

And for a rod of length L and radius r,

$$R_g = \sqrt{\frac{L^2}{12} + \frac{r^2}{2}} \quad (3)$$

The primary SiO_2 spheres have a diameter of 100–150 Å according to the manufacturer. Nominally, the primary SiO_2 fibers have a length of 400–1000 Å and a diameter of 90–150 Å. Based on these values, the radii of gyration of SiO_2 spheres and SiO_2 fibers would be 39–58 Å and 120–294 Å, respectively. As we show below, however, the two fillers are structurally very similar, with no evidence of significant rod-like character in either case and quite similar radii of gyration of 57 ± 5 Å.

The data were also analyzed by Porod analysis in the high-q region [62–64]. Specifically, the Porod pre-factor of level 1, B_1 is used to determine the interfacial area per unit sample volume, S_v:

$$B_1 = 2\pi\langle\Delta\rho\rangle^2 S_v \quad (4)$$

where $\Delta\rho$ is the contrast or difference in scattering-length-density between the filler and the matrix, which can be calculated from the chemical formula and densities of the filler and matrix. The interfacial area per unit mass of the filler is gotten from S_v using the skeletal density of the filler (see below) and the filler volume fraction φ.

In our case the data are on an absolute scale, so the Porod invariant, Q_p can be used to calculate contrast.

$$Q_p = \int_{\text{Level 1}} q^2 I(q)\mathrm{d}q = 2\pi^2\left(\Delta\rho^2\right)\varphi(1-\varphi) \quad (5)$$

If the chemical formulas of the filler and matrix are known, Q_p can be used to determine the skeletal density of the filler self-consistently, given that the density of the matrix (1.285 g/cm^3) is known. For these calculations, the chemical formula of the filler was taken to be SiO_2 and the matrix to be $C_5H_{10}O_2$. The analysis is only weakly dependent on the chemical formulas. We find a skeletal density of 2.0 ± 0.2 g/cm^3 for the fiber sample. This value is consistent with previous determinations for silica [64]. We assumed this value when analyzing the sphere data (Fig. 8(b)) because the Guinier crossover associated with the sphere primary particle is not sufficiently distinct to reliably extract Q_p.

The data were also analyzed using the fractal rod model proposed by Schaefer and Justice [65–67]. In this case, the large-scale structure is modeled as a worm-like, branched fractal cluster with a persistence length to reflect local rod-like character. This approach was used to determine if there is any evidence of short-scale linear morphology in the case of the nominally fibrous sample. As described below, however, the best fit was obtained assuming the persistence length is comparable to the rod diameter, which means that the primary particle is nearly symmetric.

3.2. Halpin–Tsai model

To interpret the modulus data we used a simplified version of the Halpin–Tsai model. According to the Halpin–Tsai model [68–72], Young's modulus of a composite can be expressed in terms of the corresponding properties of the matrix and the filler, together with their proportions and the filler geometry, using Eq. (6):

$$E_r = \frac{E_c}{E_m} = \frac{1+\xi\cdot\eta\cdot\varphi}{1-\eta\cdot\varphi}$$

and

$$\eta = \frac{\left(E_f/E_m - 1\right)}{\left(E_f/E_m + \xi\right)} \quad (6)$$

In Eq. (6), E_r is the relative Young's modulus and E_c, E_m, and E_f are the moduli of the composite, matrix, and filler, respectively; φ is the filler volume fraction. The Halpin–Tsai model assumes the filler is firmly bonded to the matrix. The factor $\xi = 2\,(L/D)$ describes the influence of the geometry of the reinforcing phase, where L/D is the aspect ratio. E_f is 80 GPa [73].

Eq. (6) assumes that the fibers are oriented. In our case, we are dealing with very short fibers that are randomly oriented. In this situation Schaefer and Justice find that Eq. (6) simplifies considerably assuming rigid fibers at low volume fraction [65]:

$$E_r = 1 + 2\left(\frac{L}{D}\right)C_a\varphi \quad (7)$$

where the angular factor, C_a is approximately 0.2 [74]. Eq. (7) is relevant to the systems studied here since it shows that large aspect ratio, L/D, is essential to fiber reinforcement. Eq. (7) assumes $L/D \gg 1$. In the limit $L/D \to 1$, the Smallwood [75] limiting law for independent spherical particles obtains, which is independent of filler size:

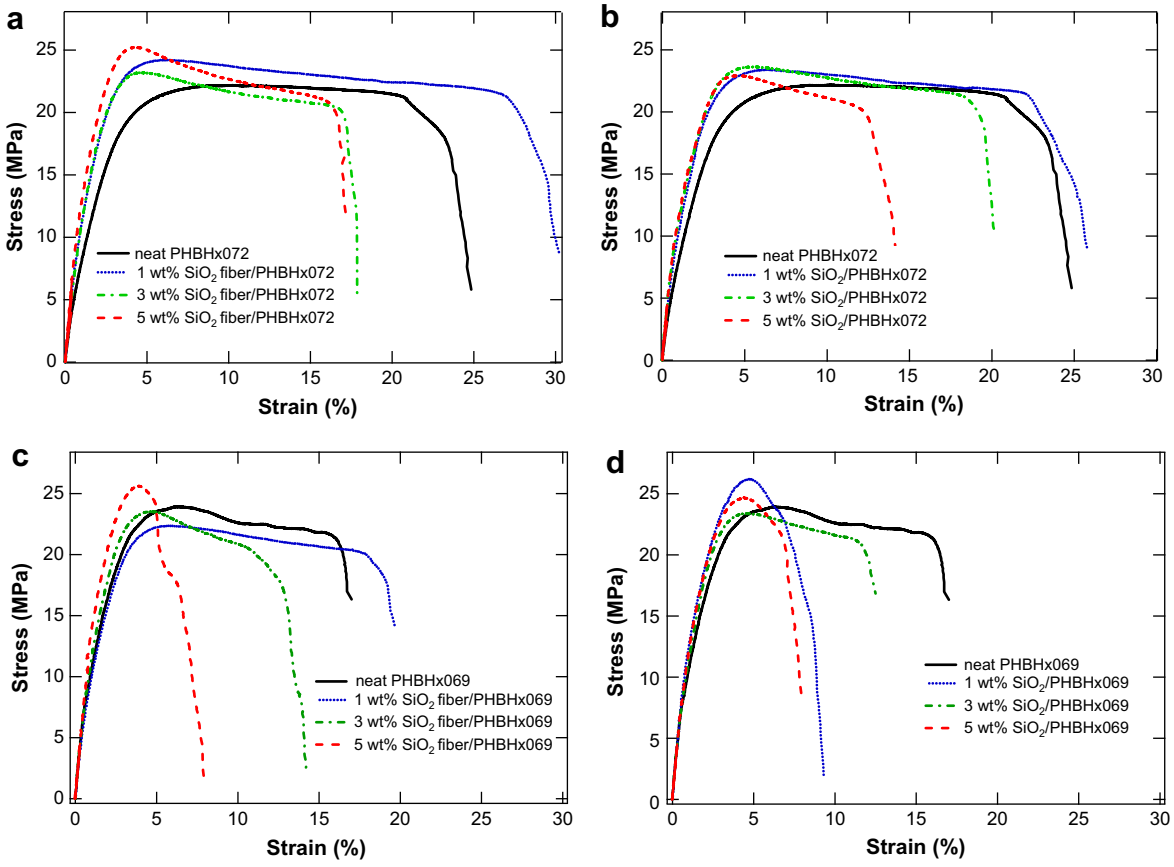

Fig. 1. Typical stress–strain curves of (a) SiO_2 fiber/PHBHx072, (b) SiO_2/PHBHx072, (c) SiO_2 fiber/PHBHx069, and (d) SiO_2/PHBHx069 nanocomposites with different filler contents.

$$E_r = 1 + 2.5\varphi \quad (8)$$

4. Results

The typical stress–strain curves of the SiO_2 fiber/PHBHx072, SiO_2/PHBHx072, SiO_2 fiber/PHBHx069 and SiO_2/PHBHx069 nanocomposites are shown in Fig. 1. For all nanocomposites, the curves show that Young's modulus increased with filler content. With the exception of the SiO_2/PHBHx069 nanocomposites, the elongation at break and toughness reached a maximum value at 1-wt% loading and then decreased with further loading. These results show that addition of SiO_2 to PHBHx069 makes this polymer more brittle (Fig. 1(d)) while improved ductility was achieved when SiO_2 fibers were added to either PHBHx matrix.

The variation of mechanical properties such as Young's modulus, ultimate strength and toughness on filler content of the PHBHx nanocomposites is shown in Fig. 2. The ultimate strength of the polymer changed little while the increase in the modulus, strain at break and toughness was matrix dependent. Compared to the unfilled polymer matrix, a 30% increase in Young's modulus and a 34% increase in toughness were obtained for the 1-wt% SiO_2 fiber/PHBHx072 nanocomposite. The addition of SiO_2 to PHBHx072 resulted in the same increase in Young's modulus (30%) but a smaller increase (11%) in toughness.

In the lower molecular weight matrix, PHBHx069, the addition of 1-wt% SiO_2 fiber also gave smaller increase (9%) in the toughness as compared to unfilled PHBHx069. When PHBHx069 was filled with SiO_2, the strain at break and toughness decreased at 1-wt% filler loading and went through a maximum at 3 wt% (Fig. 2).

In subsequent paragraphs we show that these variations in mechanical properties depend on the amorphous structure of the polymer and the filler aggregate morphology.

The morphology of tensile fracture surfaces obtained after tensile testing provides clues to the toughening mechanisms for polymers. Uniaxial tensile testing of unfilled and nanoparticle-filled PHBHx samples yielded with stress whitening bands (crazes). Fig. 3 shows the typical stress whitening after the sample reached the yield point. These bands were perpendicular to the tensile direction and throughout the gauge length. The 1-wt% SiO_2/PHBHx072 and the 1-wt% SiO_2 fiber/PHBHx072 nanocomposites fractured with

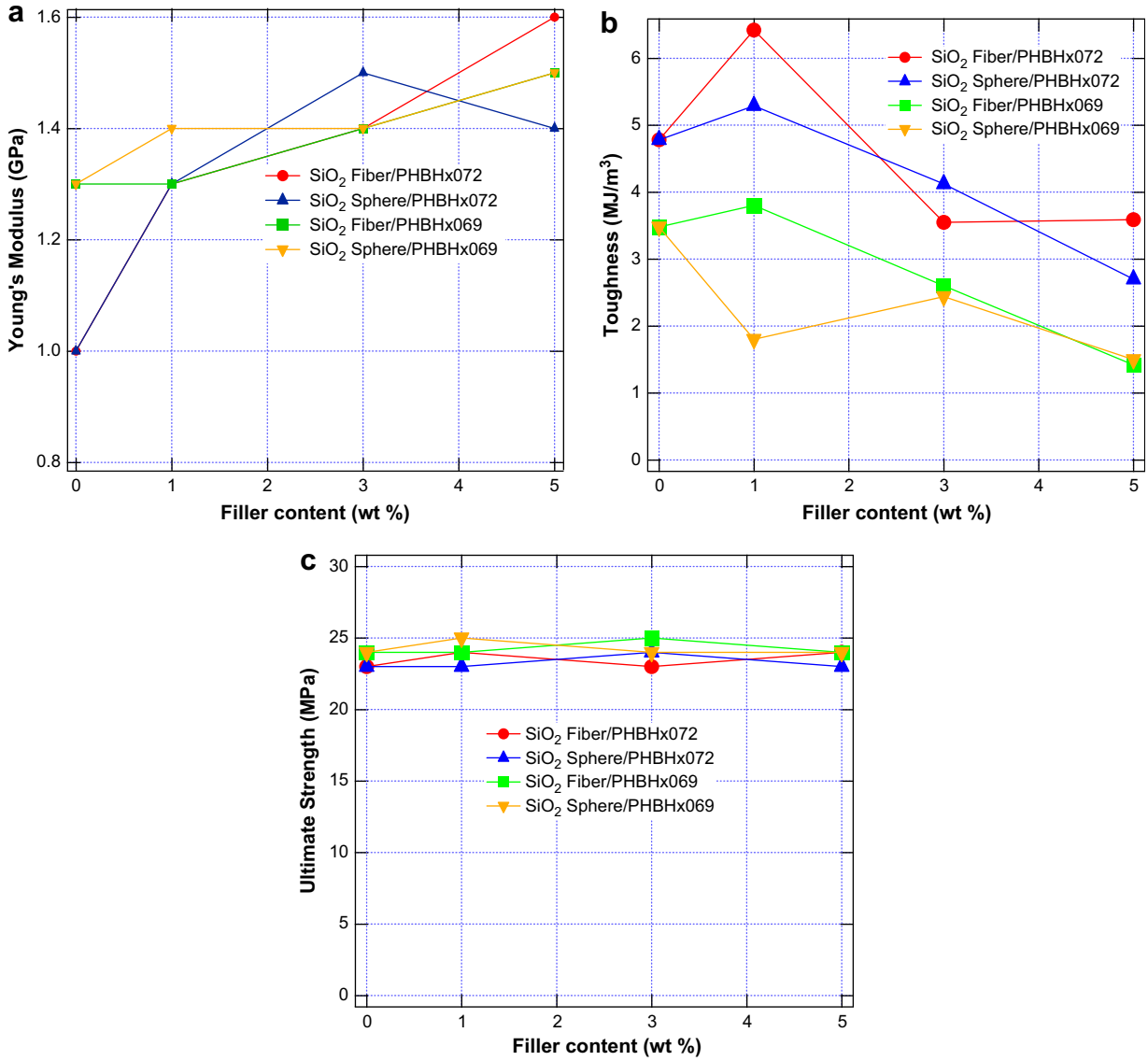

Fig. 2. Young's modulus (a), toughness (b) and ultimate strength (c) of SiO_2 fiber/PHBHx072, SiO_2 sphere/PHBHx072, SiO_2 fiber/PHBHx069 and SiO_2 sphere/PHBHx069 nanocomposites with different filler contents.

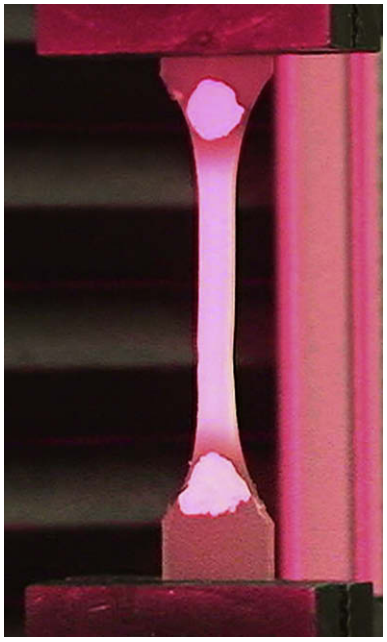

Fig. 3. A typical photo that shows the stress whitening after the yield point for all the samples tested during the tensile testing.

a slight necking. All other samples fractured without a necking, indicating that the enhancement in toughness obtained for these samples depends on the extent of shear yielding and crazing in the samples.

FESEM images (Figs. 4–6) of the morphologies of the tensile fracture surfaces after the tensile testing show that unfilled PHBHx and silica/PHBHx nanocomposites exhibit varying degrees of intensive craze-like mechanisms including cavitation and fibrillation.

The voids caused by the debondings at the particle–polymer interfaces were seen by FESEM for all the nanocomposites, especially for the PHBHx072 nanocomposites. It is worth noting that voids are seen in Fig. 4(e), (g) and (h). In comparison with PHBHx072 samples, PHBHx069 samples had fewer voids (Fig. 5). For the 5-wt% SiO_2 fiber/PHBHx069 nanocomposite, many fine cracks were found on its fracture surface (Fig. 5(j)). It is believed that the bigger agglomerates at higher loadings cannot prevent the voids from coalescing to form catastrophic cracks [76].

As with other nanocomposites [77,78], the dispersion of silica influences the mechanical properties. In the PHBHx072 nanocomposites, good dispersion of SiO_2 and SiO_2 fibers at 1 wt% loading is obtained (Fig. 6(a) and (b)) in the sense that the agglomerates are evenly distributed. As the filler content is increased, the size of the agglomerates increases and their distribution broadens. In the 3 wt% and 5 wt% nanocomposites the agglomerates are about ~1 μm in diameter (Fig. 6(c)–(f)). These large agglomerates lead to cracks in the sample as indicated by arrows (Fig. 6(c)).

To correlate the mechanical properties with filler morphology, USAXS measurements on the SiO_2/PHBHx072 and the SiO_2 fiber/PHBHx072 nanocomposites were carried out at 170 °C. USAXS provides information on the internal structure of the silica agglomerates. Since the q range of the USAXS measurements was from 0.0001 to 1 $Å^{-1}$, the size of the objects that could be detected ($2\pi/q$) was from 6 Å to 6 μm.

Fig. 7 shows the USAXS scattering cross-section per unit sample volume (called the intensity) as a function of q and the corresponding unified fits for the 1-wt%, 3-wt% and 5-wt% SiO_2/PHBHx072 (a) and SiO_2 fiber/PHBHx072 nanocomposites (b). At the smallest q region (structure level 3), all the samples showed a power-law tail with slope of about −4. Such scattering is usually seen for solid samples and probably arises from large-scale defects (dust or bubbles) in the bulk of the sample or on the surface.

Although the data in Fig. 7(a) and (b) appear quite different, detailed analysis reveals some key similarities. The radius of gyration of the primary particles is the same ($R_g = 57 \pm 6$ Å). Both systems consist of primary particles aggregated to form a second-level aggregate structure. Neither system consists of independent, dispersed spheres or rods. The key difference is the size and morphology of the level-2 aggregate. In the case of SiO_2/PHBHx072 a distinct Guinier crossover is seen in the 1 and 5-wt% samples. In the 3-w% sample the crossover is less distinct but still present. For the SiO_2 fiber/PHBHx072 sample (Fig. 7(b)), however, no crossover is seen so the aggregate size is either beyond the resolution of the instrument or masked by the parasitic scattering at very small q.

To address the filler morphology quantitatively, we examined the 5-wt% sphere and fiber/PHBHx072 samples at 170 °C in detail (Fig. 8). The data were analyzed using the unified method and the Porod method described above. In the case of the nominally fiber sample, we also fit the data with a fractal rod model in an attempt to estimate the effective aspect ratio of the filler.

Fig. 8(a) shows the analysis of the 5-wt% SiO_2 fiber/PHBHx072 at 170 °C. The low-q power-law scattering was subtracted. The plot shows a fit to the fractal rod model [65–67] as well as a 2-level unified fit assuming that the level-2 R_g is infinite.

From the unified fit, the primary particle R_g is of 56 ± 6 Å corresponding to an equivalent hard-sphere radius of 72 Å. In this case the large-scale aggregate is mass fractal in character with a fractal dimension of 2.1 ± 0.1.

Porod analysis gives a surface area per unit mass of $S_m = 285 \pm 50$ m^2/g of silica and a skeletal density of $\rho_{SiO_2} = 2.0 \pm 0.3$ g/cm^3. The corresponding equivalent sphere radius $(3/(\rho_{SiO_2} S_m))$ is 53 Å. If the primary segments are rod-like, the equivalent rod radius $(2/(\rho_{SiO_2} S_m))$ is 35 Å.

The best fit to the fractal rod model gives a persistence length (actually a half length) of 70 Å. Although the model is crude and the fit is poor, it does show that the primary particles are nearly symmetric.

The nominally spherical silica (Fig. 8(b)) differs only in the size and morphology of the aggregate. The primary particle R_g is 58 ± 10 Å, matching the fiber sample. The interfacial area, however, is 195 ± 75 m^2/g, also the same as the fiber cousin. In this case we assumed a skeletal density of 2.0 g/cm^3, because the primary particle scattering is not sufficiently distinct to extract the Porod invariant.

The agglomerate is more compact and much smaller for the sphere sample. The fractal dimension is 2.8 ± 0.2 as compared with 2.1 ± 0.1 for the fiber case. More importantly, the aggregates are quite small with an R_g of 662 ± 40 Å and an aggregation number of 11.

These results indicate that the improved performance of the fiber-type fillers is due to the larger more open aggregate morphology. Although we cannot determine the size or aggregation number of the fiber filler from the USAXS data we can say that the size is greater than 5000 Å and the aggregation number is greater than 1×10^4.

The physical and mechanical properties of polymer nanocomposites depend on the strength/type of interaction between the filler and the matrix, and the crystalline and the spherulitic structures of the matrix. To investigative the influence of silica on the thermal properties and crystalline structure of PHBHx matrices, DSC cooling and melting (Figs. 9 and 10) measurements were performed.

In our silica/PHBHx nanocomposites, the glass transition temperature (T_g) for all the samples was the same (8 ± 1 °C) (Figs. 9(a) and

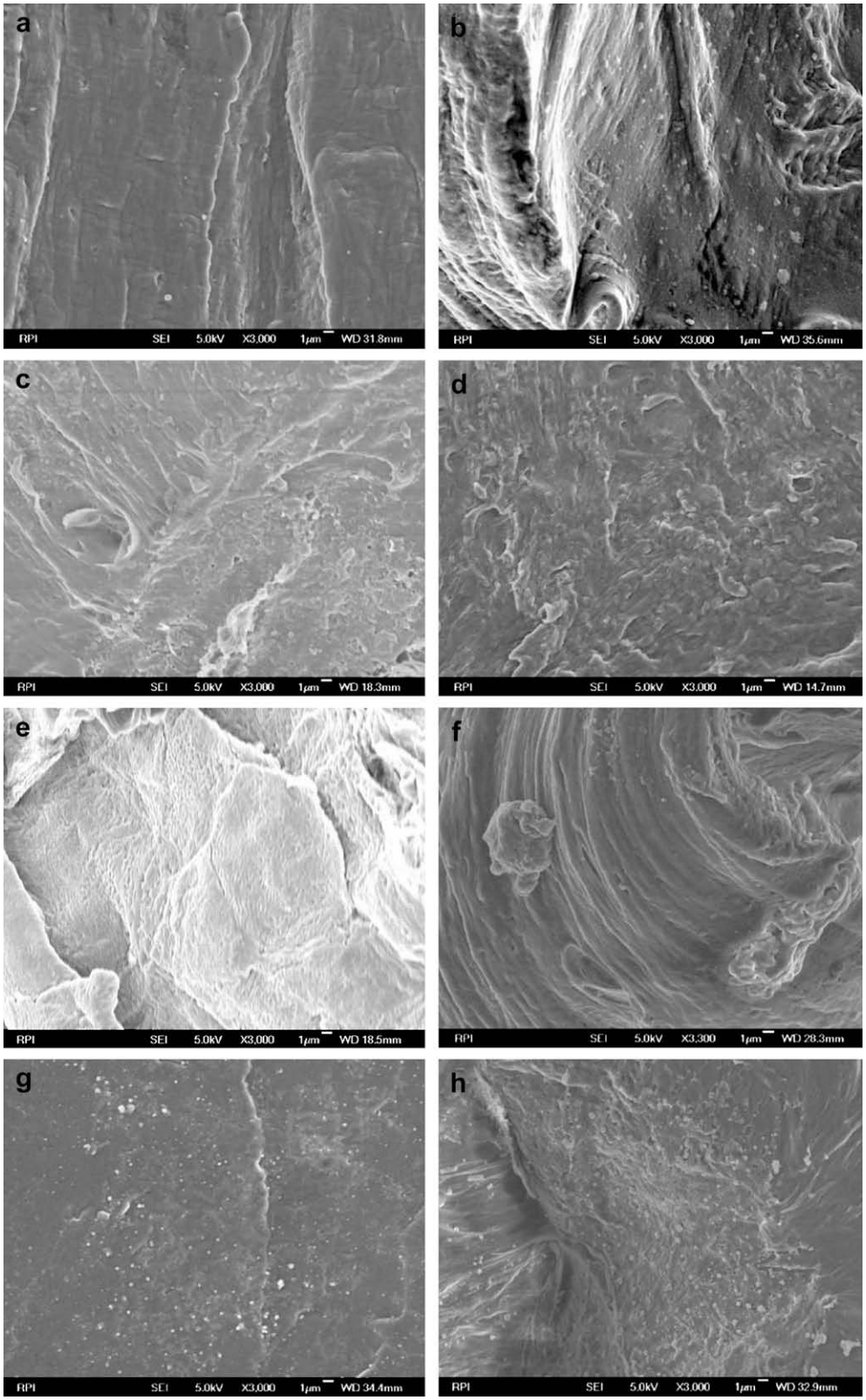

Fig. 4. SEM micrographs of the fracture surfaces of tensile specimens: (a) neat PHBHx072, (b) 1 wt% SiO_2, (c) 3 wt% SiO_2, (d) 5 wt% SiO_2, (e) lots of nanovoids in 3 wt% SiO_2, (f) 1 wt% SiO_2 fiber, (g) 3 wt% SiO_2 fiber, and (h) 5 wt% SiO_2 fiber.

10(a)). Increases in T_g have been attributed to attractive interaction between the filler and the polymer; depression of T_g is found when the interface between filler and polymer is weak [79,80]. Since T_g did not change, there were no strong attractive or repulsive interactions between the nanoparticles and the polymers. Therefore, the interfacial adhesion between them must be weak.

As with other crystalline polymers, the addition of nanofillers to PHBHx can be used to control the crystallization behavior and

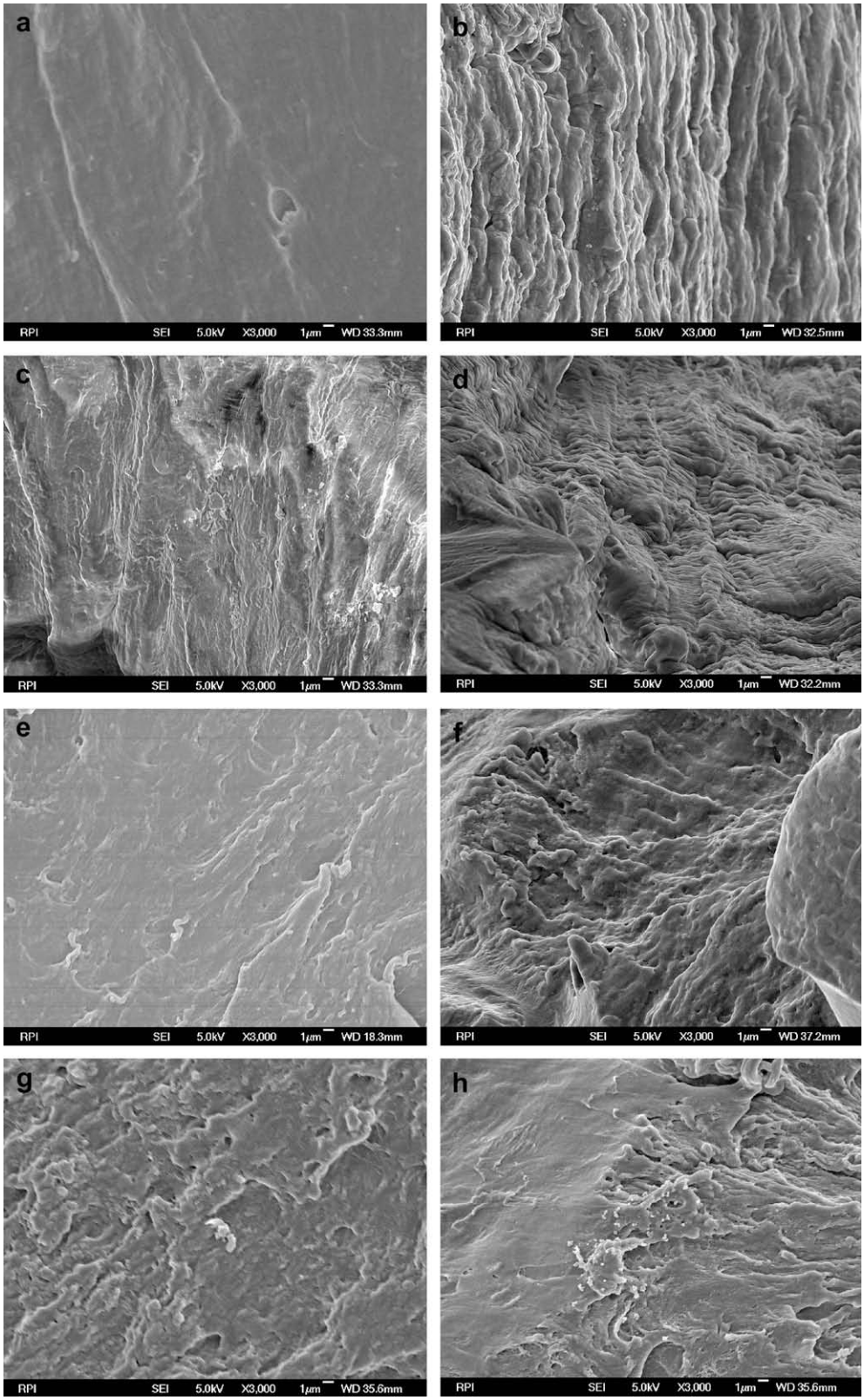

Fig. 5. SEM micrographs of the fracture surfaces of tensile specimens: (a) neat PHBHx069, (b) 1 wt% SiO_2, (c) and (d) 1 wt% SiO_2 fiber, (e) 3 wt% SiO_2, (f) 3 wt% SiO_2 fiber, (g) and (h) 5 wt% SiO_2, and (i) and (j) 5 wt% SiO_2 fiber. The arrows point to the cracks formed in the sample.

resulting morphology. Nanoparticles can change the lamellae size [81], spherulitic structure [82–89] degree of crystallinity [90] and rate of crystallization [91–94]. Nanoparticles can also suppress the formation of the thermodynamic crystal phase and stabilize the metastable phase [90]. Recently Giannelis and co-workers have demonstrated the enhanced crystallization rate in clay–PHB composites [91]. Our silica/PHBHx nanocomposites show similar behavior.

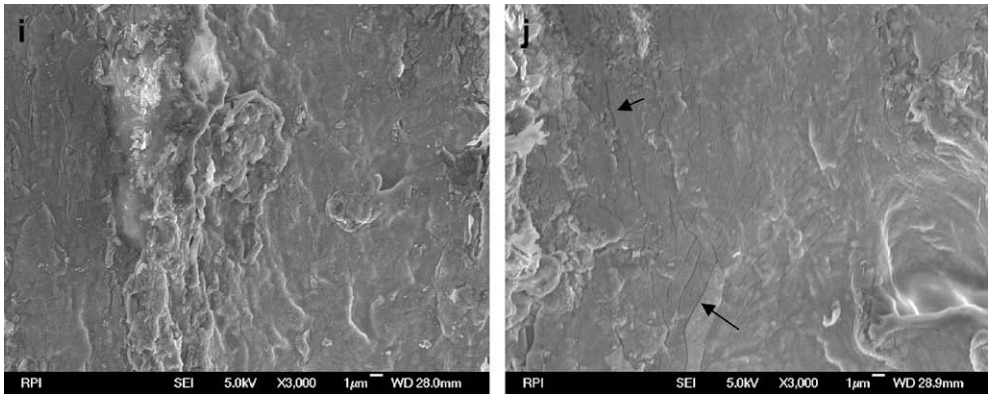

Fig. 5. (*continued*).

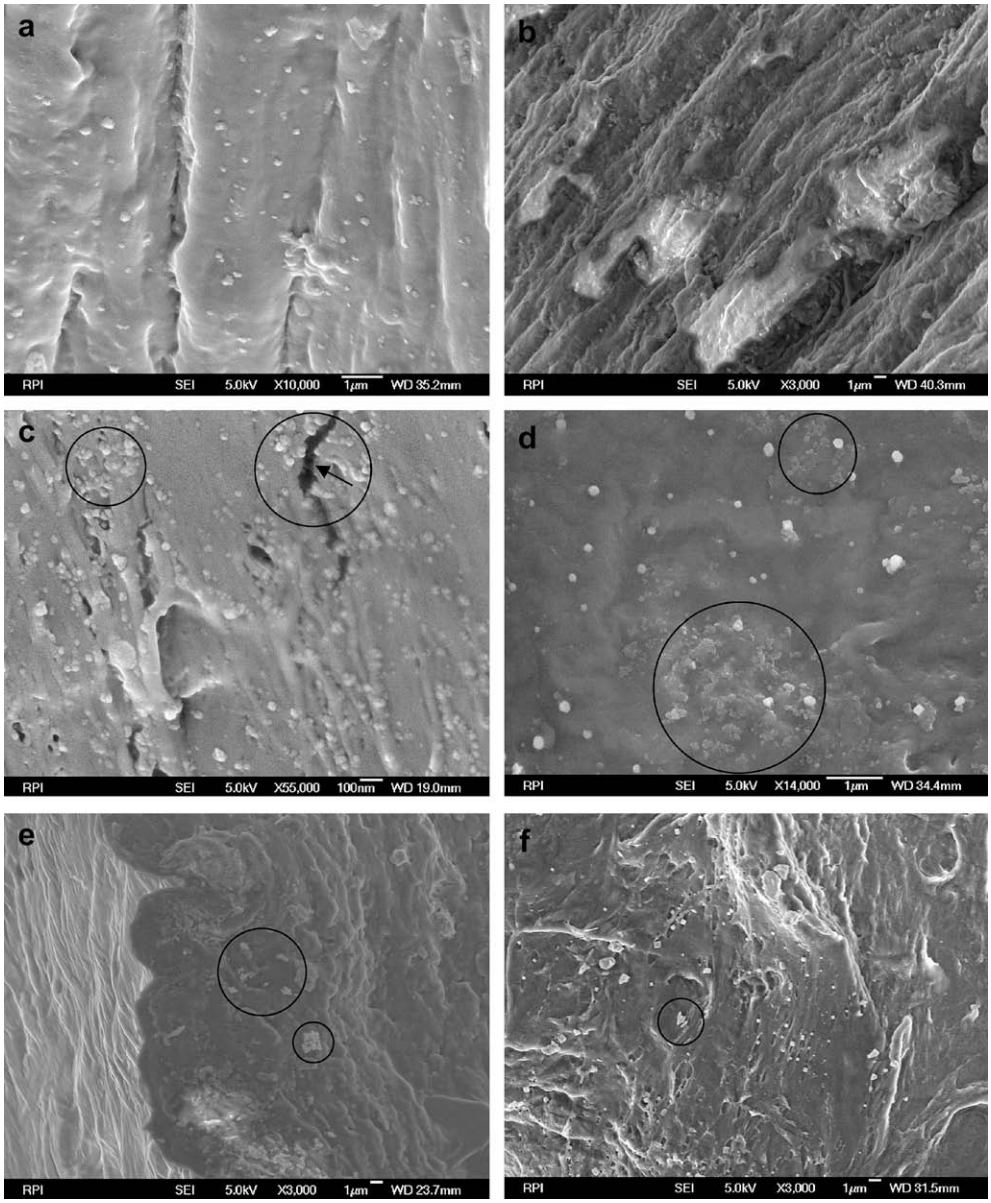

Fig. 6. SEM micrographs of the fracture surfaces of PHBHx072 nanocomposites: (a) 1 wt% SiO_2, (b) 1 wt% SiO_2 fiber, (c) 3 wt% SiO_2, (d) 3 wt% SiO_2 fiber, (e) 5 wt% SiO_2, and (f) 5 wt% SiO_2 fiber. The circles represent the agglomerations of the nanoparticles and the arrow points to a crack formed in the sample.

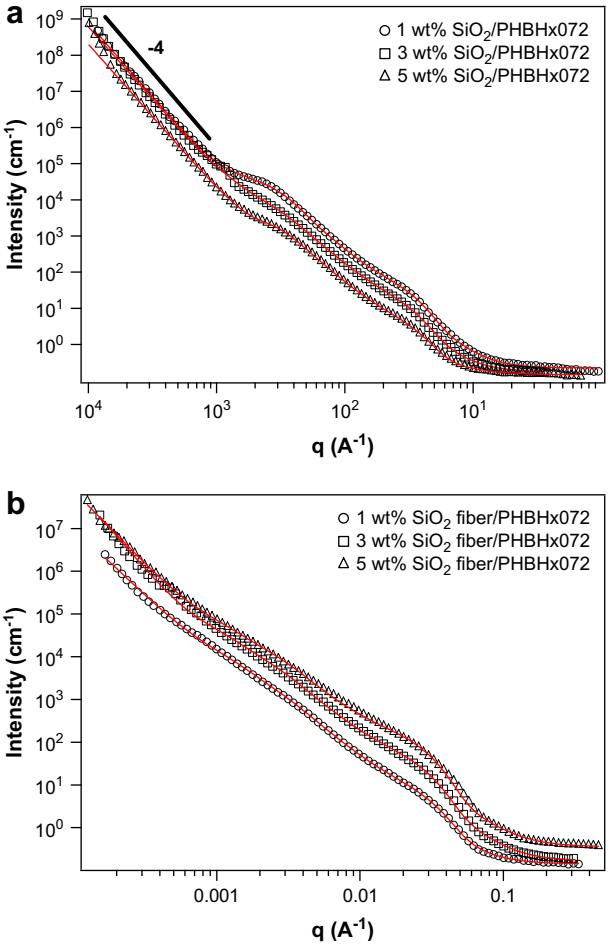

Fig. 7. USAXS scattering profiles for (a) the SiO_2/PHBHx072 nanocomposites with 1 wt%, 3 wt% and 5 wt% SiO_2, and (b) the SiO_2 fiber/PHBHx072 nanocomposites with 1 wt%, 3 wt% and 5 wt% SiO_2 fiber. The solid lines are unified fits. Although the data look qualitatively different, the basic morphology is very similar except for the size of the second-level aggregate structure.

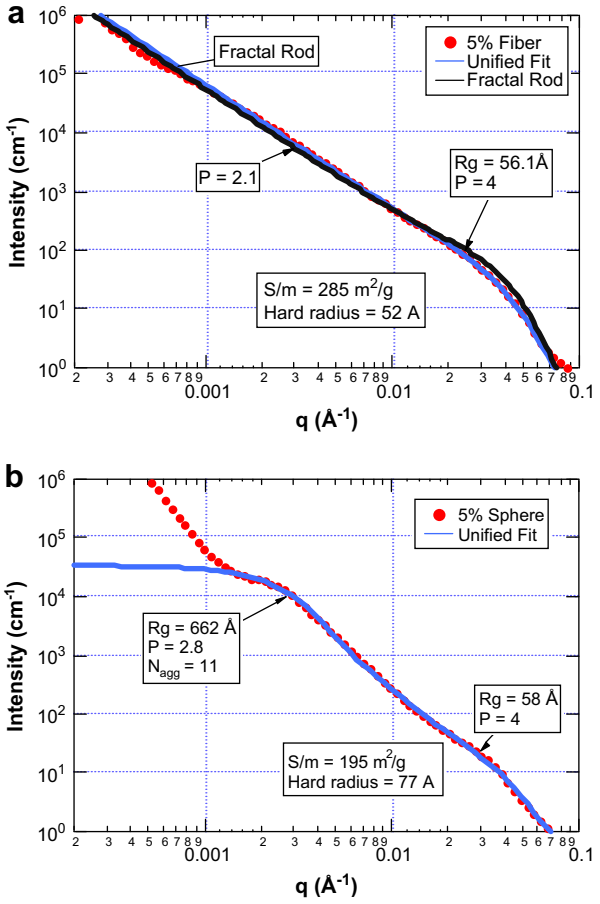

Fig. 8. (a) Analysis of USAXS data for the 5-wt% SiO_2 fiber/PHBHx072 at 170 °C. The R_g from the unified fit of 56 ± 10 Å is essentially the same as that for the sphere sample. The primary particles are aggregated as a mass fractal of dimension 2.1 ± 0.1 and the size of the aggregate exceeds 0.5 μm. The fractal rod model gives a persistence length of 70 Å, only slightly larger than the rod radius calculated from the surface area. The key difference between the fiber and sphere samples is the nature of the aggregate, which is much large and more open (lower fractal dimension) than the sphere sample. "*P*" is the Porod slope, which is equal to the mass fractal dimension in the aggregate regime. The surface area/unit mass of the filler (S/m) is gotten from Porod analysis of the high-q region. (b) Analysis of USAXS data for the 5-wt% SiO_2 sphere/PHBHx072 at 170 °C. The R_g from the unified fit of 58 ± 6 Å is essentially the same as that for the fiber sample. In this case, however, the primary particles are aggregated as a mass fractal of dimension 2.8 ± 0.1 and the size of the aggregate is 662 ± 80 Å. The aggregation number ($N_{agg} = 11$) is at least 1000 times smaller than the fiber in (a). The surface area/unit mass of the filler (S/m) is gotten from Porod analysis of the high-q region.

For all the silica/PHBHx nanocomposites studied, the addition of the silica fibers or the silica spheres did not change the peak or the final melting temperatures significantly (Table 3), indicating that the crystal structures did not change, although the degree of crystallinity decreased slightly. During cooling, a crystallization peak was observed at about 95 °C for the 1 °C/min cooling rate (Figs. 9(b) and 10(b)). During the subsequent heating, a cold crystallization peak was not observed (Figs. 9(a) and 10(a)).

Unfilled PHBHx069 had a slightly higher degree of crystallinity ($X_c = 50\%$) than the unfilled PHBHx072 ($X_c = 48\%$). The peak crystallization temperature ($T_c^p = 96.3$ °C) and the onset crystallization temperature ($T_c^{onset} = 105.5$ °C) of the neat PHBHx069 were higher than those of the neat PHBHx072, indicating that the crystallization rate of the neat PHBHx069 was faster than that of the neat PHBHx072.

For the PHBHx072 materials at 5-wt% loading the degree of crystallinity is reduced from 48% to 43%, a 5% reduction. If the particles reduced the crystallinity in a halo region of dimension x, x can be calculated from the surface area per unit volume measured by USAXS ($S_v = 16\ m^2/cm^3$ for 5-wt% fiber) as $0.05/(X_c S_v) = 8$ nm. Given that the long period (L) is about 6 nm, and the average size of the crystalline and amorphous phases is about 3 nm, the reduction of crystallinity is accounted for by minimal alteration of the interface region between lamellar stacks and spherulites. In other words, because of the large interfacial area, the impact of nanoparticles is large even though the halo region is small.

With the same filler loading, the SiO_2 fiber nanocomposites always had a lower T_c^{onset} and a lower T_c^p than the corresponding SiO_2 nanocomposites, indicating that the silica spheres accelerated the crystallization more than the silica fibers (Table 3). USAXS shows that the S_v for spheres is comparable to that for fibers ($13 \pm 3\ m^2/cm^3$ vs. $16 \pm 3\ m^2/cm^3$ at 5-wt% loading), so the small change in crystallinity is not likely due to a nucleation effect. The 1-wt% and 3-wt% SiO_2/PHBHx072 nanocomposites had a faster crystallization rate than the neat polymer, but the 5-wt% SiO_2/PHBHx072 nanocomposite had a slower crystallization rate. For the SiO_2 fiber/PHBHx072 nanocomposites, high filler concentrations (3-wt% and 5-wt%) also reduced the rate of crystallization. Similar effects have been observed for nanocomposites in other matrices like nylon 6 [95] and poly(ε-caprolactone) systems [96].

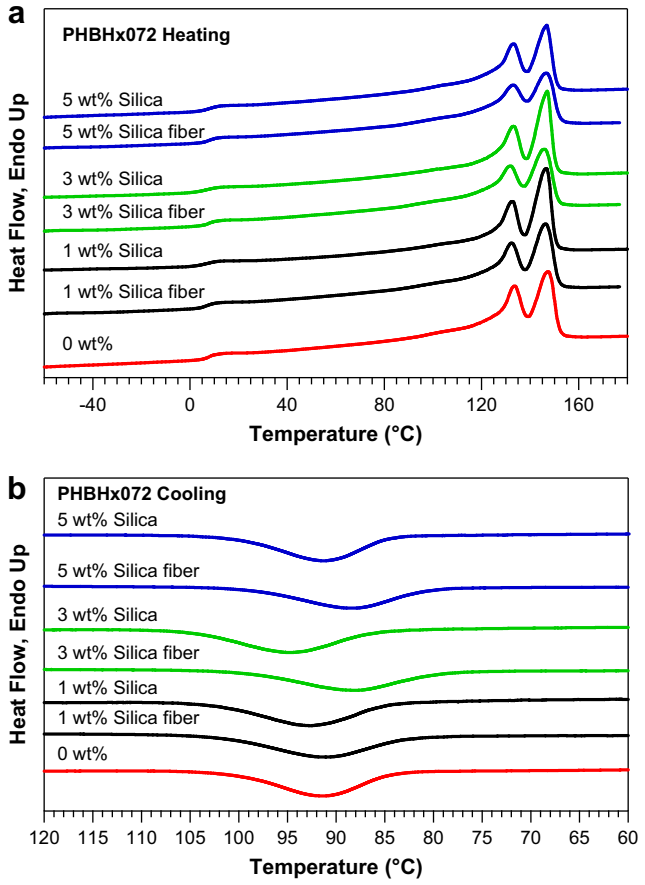

Fig. 9. DSC heating scans (a) and cooling scans (b) of neat PHBHx072 and its nanocomposites with different filler contents. Samples were cooled from a melt to −80 °C at a rate of 1 °C/min. Scans are shifted for clarity.

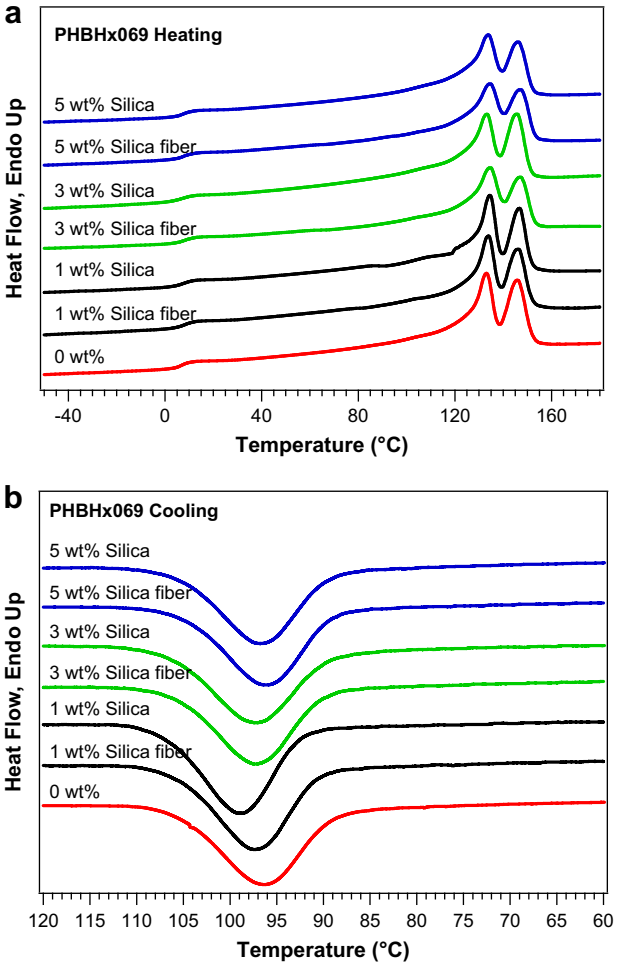

Fig. 10. DSC heating scans (a) and cooling scans (b) of neat PHBHx069 and its nanocomposites with different filler contents. Samples were cooled from a melt to −80 °C at a rate of 1 °C/min. Scans are shifted for clarity.

The acceleration of crystallization at low and intermediate loadings can be explained by the two roles that the nanofillers play in the crystallization: nucleation facilitating the crystallization and physical hindrance slowing growth [71,97,98]. At low concentrations, the distance between dispersed particles is large so it is relatively easy for the additional nucleation sites to incorporate the surrounding polymer. At high concentrations, however, diffusion of polymer chains to the growing crystallite is hindered.

The effect of silica nanoparticles on the spherulitic morphologies of PHBHx072 was studied by POM. The dark regions (or more precisely, less contrast regions) in Fig. 11(a), are actually spherulites with much smaller sizes, which were verified by DSC (crystallinity) and small-angle light scattering (data not shown in the manuscript). Thus at a moderate (10 °C/min) (Fig. 11(a)) cooling rate, the average spherulite size decreased significantly with filler content. However, at a slow (1 °C/min) cooling rate (Fig. 11(b)), there was no significant change of the average size ($\sim 500 \pm 200$ μm) and texture of the spherulites after adding silica nanoparticles into the polymer matrix. Therefore, the spherulitic morphologies obtained at 1 °C/min cooling rate suggest that the cooling rate rather than the nucleating agents dominated the growth of the spherulites.

TGA shows that the thermal stability of PHBHx is also improved by addition of silica (Fig. 12). The effect of filler content on the weight loss of the nanocomposites was deduced from the temperature at 50% weight loss of polymer.

The temperatures at 50 wt% weight loss of neat PHBHx072, 5-wt% SiO_2/PHBHx072 and 5-wt% SiO_2 fiber/PHBHx072 nanocomposites were 294.2 °C, 297.4 °C and 299.5 °C, respectively. Therefore, the thermal stability of the polymer was slightly improved by the addition of nanofillers, indicating that the nanofillers were effective barriers to the heat and mass transport.

5. Discussion

The mechanical properties of polymer nanocomposites can be affected by many factors, such as the interaction between particles and a polymer matrix, crystallinity of the polymer, spherulitic morphology, molecular weight of the polymer matrix, dispersion state of the particles in the polymer matrix, etc.

Matrix characteristics do not change significantly in the nanocomposites. From the DSC data, the transition temperature (T_g) for all the samples did not change, indicating that there are no strong attractive or repulsive interactions between the nanoparticles and the polymers. Therefore, the interfacial adhesion between them must be weak. In addition, changes in degree of crystallinity and spherulitic morphology caused by the addition of filler are minimal at 1 °C/min cooling rate. From the tensile testing results, the neat PHBHx069 is stiffer but less ductile than the neat PHBHx072.

The major difference between the neat PHBHx072 and the neat PHBHx069 is their molecular weights. Fornes and co-workers [95,99–101] studied the effect of molecular weight on the mechanical properties of nylon 6 organoclay nanocomposites. They found that neat nylon 6 with lower molecular weight ($M_n = 16{,}400$)

Table 3
Thermal properties of neat PHBHx072, neat PHBHx069 and their nanocomposites cooled from a melt at 1 °C/min, obtained from the analysis of the DSC data.

Samples	T_m^p(°C)	T_m^f(°C)	ΔH_m (J/g)	X_c (%)	T_c^{onset} (°C)	T_c^p (°C)	ΔH_c (J/g)
Neat PHBHx072	133.5, 147.4	152.0	54.8	48	101.8	91.4	45.5
1 wt% SiO_2 fiber/PHBHx072	132.6, 146.2	152.0	50.7	45	102.1	91.1	47.2
1 wt% SiO_2/PHBHx072	132.6, 146.7	150.6	53.3	47	104.6	92.6	49.1
3 wt% SiO_2 fiber/PHBHx072	131.8, 145.8	151.7	46.3	42	99.6	88.1	44.7
3 wt% SiO_2/PHBHx072	133.2, 147.1	151.1	49.4	44	104.8	94.8	48.5
5 wt% SiO_2 fiber/PHBHx072	133.2, 146.6	152.7	46.6	43	98.9	88.3	41.9
5 wt% SiO_2/PHBHx072	133.2, 146.8	151.2	47.1	43	100.4	91.3	47.2
Neat PHBHx069	133.1, 146.0	152.7	57.3	50	105.5	96.3	47.3
1 wt% SiO_2 fiber/PHBHx069	133.8, 146.3	152.7	53.0	46	105.8	97.4	47.9
1 wt% SiO_2/PHBHx069	134.5, 146.7	152.5	52.9	46	107.4	98.8	47.8
3 wt% SiO_2 fiber/PHBHx069	134.6, 147.0	153.0	52.8	47	105.9	97.3	45.9
3 wt% SiO_2/PHBHx069	133.3, 145.6	151.5	53.2	48	105.9	97.3	45.3
5 wt% SiO_2 fiber/PHBHx069	134.6, 147.0	153.1	52.9	48	104.8	96.1	42.5
5 wt% SiO_2/PHBHx069	133.8, 146.3	152.3	52.3	48	105.7	96.7	43.1

had higher Young's modulus and less ductility than the higher molecular weight ($M_n = 29{,}300$). In general, decreasing the molecular weight results in a faster crystallization, which is to be expected on the basis of mobility considerations and has been observed for many polymers [102]. Although we do observe higher crystallinity in the lower molecular weight sample (PHBHx069), the difference is only 2%.

Stress whitening is seen in all samples. Plastic tensile deformation of crystalline polymers can cause cavitation, producing sudden polymer whitening near the yield point [21]. Michler et al. [21] studied the influence of molecular weight on the micromechanical deformation and found that their significant differences are connected with the decreasing thickness of the amorphous material between lamellae with decreasing molecular weight. Fewer tie

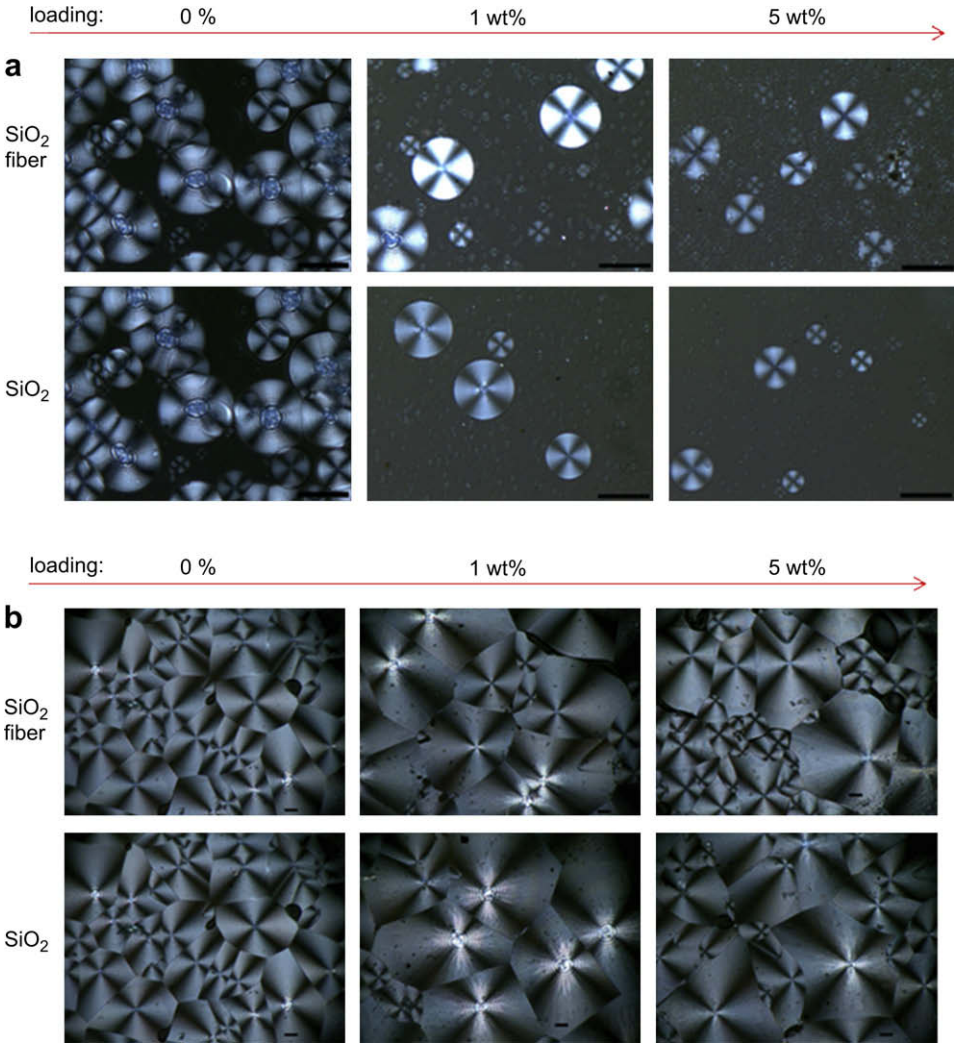

Fig. 11. The effect of filler content (0, 1 and 5 wt%) on the spherulitic morphologies of PHBHx072 samples that were cooled from a melt with (a) 10 °C/min cooling rate, (b) 1 °C/min cooling rate. The scale bar = 100 μm.

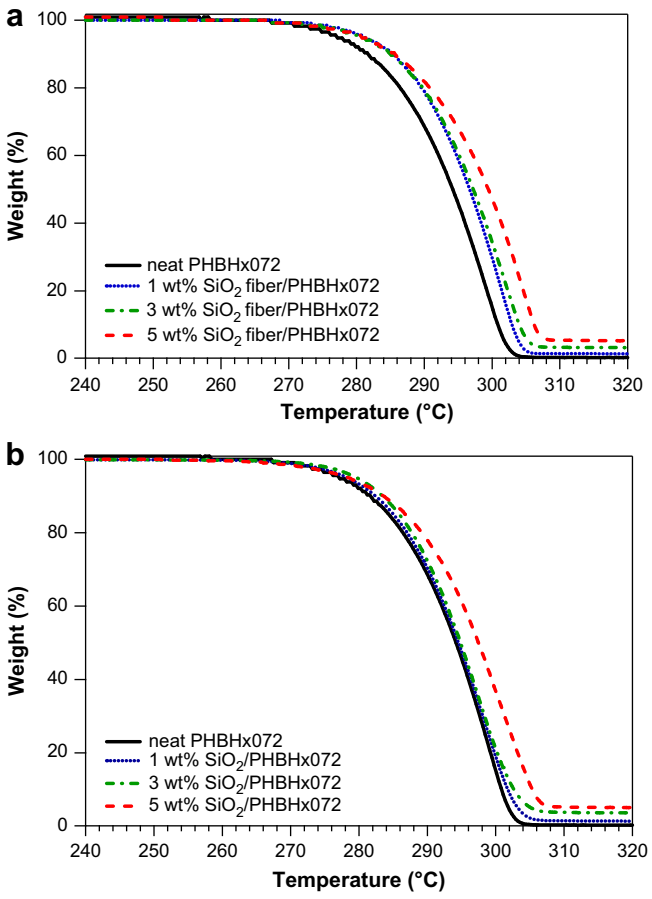

Fig. 12. TGA curves for (a) neat PHBHx072 and its nanocomposites with different contents of SiO_2 fibers, and (b) PHBHx072 and its nanocomposites with different contents of SiO_2 spheres.

molecules or entanglements between lamellae exist at lower molecular weights. Cavitation in the amorphous phase, therefore, cannot be stabilized and local stress concentrations result in longer crazes and a transition from ductile to quasi-brittle behavior [21].

If the interfacial adhesion is not high, debonding at the particle–polymer interface can occur, leading to crazing and/or shear yielding [21,76,103]. In our case, this mechanism may have been active in the 1 wt% SiO_2/PHBHx072 and 1 wt% SiO_2 fiber/PHBHx072 nanocomposites, which fractured with a slight necking that led to a more ductile behavior.

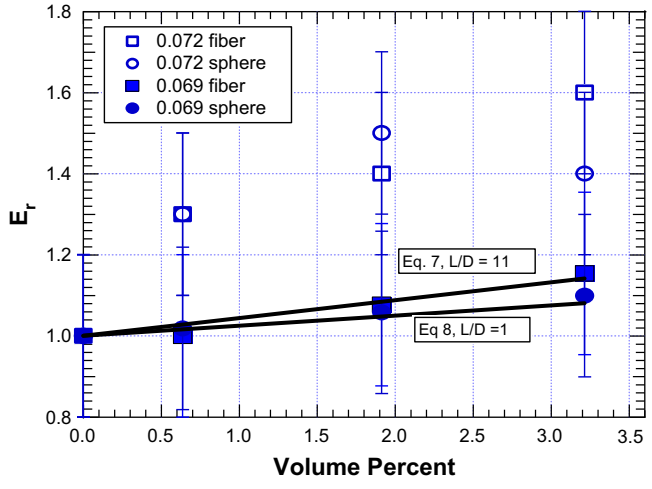

Fig. 13. Measured relative modulus compared to the prediction for reinforcement with symmetric and asymmetric particles. The 072 matrix seems to give anonymously large reinforcement.

Although void formation is a secondary factor contributing to toughness (in other words, only a small part of energy dissipation may contribute to toughness), it plays an important role for the activation of further plastic deformation [104]. When filler loading is low (1 wt%) the formation of nanovoids releases strain constraints and induces local shear deformation in polymer ligaments between nanoparticles. As loading increases, however, the aggregates act as flaws, which trigger brittle response and premature material failure before the shear yielding is able to start.

In principle modulus should be less sensitive to defects and therefore easier to interpret. In our case, however, the modulus is strongly dependent on the matrix, which, based on the above results, is nearly the same for the two polymers. Fig. 13 shows the experimental values of $E_r = E_c/E_m$ and the predictions based on the simplified Halpin–Tsai model (Eqs. (7) and (8)). Based on the USAXS results, the primary particles are nearly symmetric so Eq. (8) should be applicable. Even if the extreme value of the aspect ratio from Nissan is assumed ($L/D = 11$) the prediction changes little. Both predictions agree with the 069 data, but fall outside the error bars for the 072 data.

Eqs. (7) and (8) assume independent, rigid particles so that the elastic energy is stored in the strain field around the particles. In principle these equations could be altered for aggregated particles. Interactions between the strain fields of the primary particles would alter these simple predictions. Also Eq. (8) represents the minimum expected reinforcement because it neglects energy stored in the filler itself [65]. Since we observe no difference in modulus enhancement for the spheres and fibers, which differ dramatically in the nature of the aggregate, it seems like these compromising factors are not relevant.

Some insight into the anomalous modulus enhancement for the PHBHx072 material comes from the observation that the enhancement would be "normal" if the modulus of the unfilled materials was under estimated by 30%. That is if the modulus of the filled samples is extrapolated to zero loading, the intercept is too high by about 30%. This observation leads us to believe that the enhancement is due the impact of the filler particles on the matrix. Given that a semicrystalline polymer is itself a composite consisting of a stiff crystalline regions and more elastic amorphous regions, simple 2-component micromechanical models like Halpin–Tsai may not be adequate to account for observed enhancement. It seems that in this case, the particles would enhance the modulus of the amorphous regions more than the crystalline regions. Being less crystalline the PHBHx072 sample is therefore more susceptible to enhancement.

6. Conclusions

Simultaneous improvement of both stiffness and toughness was observed at 1 wt% loading of SiO_2 spheres or SiO_2 fibers for the higher molecular weight PHBHx matrix. The SiO_2 fibers had a greater toughening effect than SiO_2 spheres. When the loading was 3 wt% and above, Young's modulus continued to increase, but the strain at break and toughness decreased. The ultimate strength did not change for all the nanocomposites compared with the unfilled polymer.

The improvement of the mechanical properties observed was not caused by the change of crystallinity or spherulitic morphology. Instead, a sufficiently high molecular weight of the polymer matrix, weak interfacial adhesion and a good dispersion of the nanofillers are necessary to improve toughness and stiffness simultaneously.

Acknowledgements

This research was supported by the US Department of Energy, Office of Basic Energy Sciences (Grant No. FG02-06ER46349). The USAXS data were collected at the X-ray Operations and Research beamline 32-ID-B, located at the Advanced Photon Source, Argonne National Laboratory. The use of the Advanced Photon Source was supported by the US Department of Energy, Office of Science, Office of Basic Energy Sciences, under Contract No. DE-AC02-06CH11357.

References

[1] Williams CK, Hillmyer MA. Polymer Reviews 2008;48(1):1–10.
[2] Akiyama M, Tsuge T, Doi Y. Polymer Degradation and Stability 2003;80(1):183–94.
[3] Madison LL, Huisman GW. Microbiology and Molecular Biology Reviews 1999;63(1):21–53.
[4] Anderson AJ, Dawes EA. Microbiological Reviews 1990;54(4):450–72.
[5] Smith R. Biodegradable polymers for industrial applications. Boca Raton: CRC Press LLC; 2005.
[6] Chen GQ, Wu Q. Biomaterials 2005;26(33):6565–78.
[7] Wang YW, Wu QO, Chen JC, Chen GQ. Biomaterials 2005;26(22):4693.
[8] Noda I. Films comprising biodegradable PHA copolymers. US Patent No. 6,174,990; 2001.
[9] Noda I, Green PR, Satkowski MM, Schechtman LA. Biomacromolecules 2005;6(2):580–6.
[10] Zini E, Focarete ML, Noda I, Scandola M. Composites Science and Technology 2007;67(10):2085–94.
[11] Hassan MK, Abou-Hussein R, Zhang XJ, Mark JE, Noda I. Molecular Crystals and Liquid Crystals 2006;447:341–62.
[12] Xie YP, Noda I, Akpalu YA. Journal of Applied Polymer Science 2008;109(4):2259–68.
[13] Tullo A. Chemical and Engineering News 2008;86(39):21–5.
[14] Sato H, Dybal J, Murakami R, Noda I, Ozaki Y. Journal of Molecular Structure 2005;744–747:35–46.
[15] Asrar J, Valentin HE, Berger PA, Tran M, Padgette SR, Garbow JR. Biomacromolecules 2002;3(5):1006–12.
[16] Freier T. Biopolyesters in tissue engineering applications. Polymers for Regenerative Medicine 2006:1–61.
[17] Williams SF, Martin DP, Horowitz DM, Peoples OP. International Journal of Biological Macromolecules 1999;25(1–3):111–21.
[18] Yang XS, Zhao K, Chen GQ. Biomaterials 2002;23(5):1391–7.
[19] Zhao K, Yang X, Chen GQ, Chen JC. Journal of Materials Science: Materials in Medicine 2002;13(9):849–54.
[20] Yoshie N, Menju H, Sato H, Inoue Y. Macromolecules 1995;28(19):6516–21.
[21] Michler GH, Balta-Calleja FJ. Mechanical properties of polymers based on nanostructure and morphology. Boca Raton: CRC Press; 2005.
[22] Vaia RA, Giannelis EP. MRS Bulletin 2001;26(5):394–401.
[23] Pinnavaia TJ, Beall GW. In: Pinnavaia TJ, Beall GW, editors. Polymer–clay nanocomposites. Chichester, England; New York: Wiley; 2000. p. 349.
[24] Giannelis EP. Advanced Materials 1996;8(1):29.
[25] Vollenberg PHT, Heikens D. Polymer 1989;30(9):1656–62.
[26] Vollenberg PHT, Dehaan JW, Vandeven LJM, Heikens D. Polymer 1989;30(9):1663–8.
[27] Sternstein SS, Zhu AJ. Macromolecules 2002;35(19):7262–73.
[28] Mitchell CA, Bahr JL, Arepalli S, Tour JM, Krishnamoorti R. Macromolecules 2002;35(23):8825–30.
[29] Ash BJ, Siegel RW, Schadler LS. Macromolecules 2004;37(4):1358–69.
[30] He CB, Liu TX, Tjiu WC, Sue HJ, Yee AF. Macromolecules 2008;41(1):193–202.
[31] Zini E, Baiardo M, Armelao L, Scandola M. Macromolecular Bioscience 2004;4(3):286–95.
[32] Singh S, Mohanty AK, Sugie T, Takai Y, Hamada H. Composites Part A: Applied Science and Manufacturing 2008;39(5):875–86.
[33] Bordes P, Pollet E, Bourbigot S, Averous L. Macromolecular Chemistry and Physics 2008;209(14):1473–84.
[34] Lim JS, Noda I, Im SS. Polymer 2007;48(9):2745–54.
[35] Maiti P, Batt CA, Giannelis EP. Biomacromolecules 2007;8(11):3393–400.
[36] Maiti P, Yadav PJP. Journal of Nanoscience and Nanotechnology 2008;8(4):1858–66.
[37] Hsu SF, Wu TM, Liao CS. Journal of Polymer Science, Part B: Polymer Physics 2007;45(9):995–1002.
[38] Bruzaud S, Bourmaud A. Polymer Testing 2007;26(5):652–9.
[39] Sanchez-Garcia MD, Gimenez E, Lagaron JM. Journal of Applied Polymer Science 2008;108(5):2787–801.
[40] Choi WM, Kim TW, Park OO, Chang YK, Lee JW. Journal of Applied Polymer Science 2003;90(2):525–9.
[41] Sato H, Murakami R, Padermshoke A, Hirose F, Senda K, Noda I, et al. Macromolecules 2004;37(19):7203–13.
[42] Sato H, Nakamura M, Padermshoke A, Yamaguchi H, Terauchi H, Ekgasit S, et al. Macromolecules 2004;37(10):3763–9.
[43] He J-D, Cheung MK, Yu PH, Chen G-Q. Journal of Applied Polymer Science 2001;82(1):90–8.
[44] Iwata T, Doi Y. Bio-based polymers. Macromolecular Symposia 2005;224:11–9.
[45] Noda I, Satkowski MM, Dowrey AE, Marcott C. Polymer alloys of Nodax copolymers and poly(lactic acid). Wiley-VCH Verlag Gmbh; 2004. p. 269–75.
[46] Fischer JJ, Aoyagi Y, Enoki M, Doi Y, Iwata T. Polymer Degradation and Stability 2004;83(3):453–60.
[47] Abe H, Doi Y. RIKEN Review 2001;42:7–10.
[48] Abe H, Doi Y. Biomacromolecules 2002;3(1):133–8.
[49] Abe H, Doi Y, Aoki H, Akehata T. Macromolecules 1998;31(6):1791–7.
[50] Abe H. Macromolecular Bioscience 2006;6(7):469–86.
[51] Sen S, Xie Y, Bansal A, Yang H, Cho K, Schadler LS, et al. European Physical Journal – Special Topics 2007;141:161–5.
[52] Sen S, Xie YP, Kumar SK, Yang HC, Bansal A, Ho DL, et al. Physical Review Letters 2007;98(12):128301–4.
[53] Bansal A, Yang HC, Li CZ, Cho KW, Benicewicz BC, Kumar SK, et al. Nature Materials 2005;4(9):693–8.
[54] Bansal A. PhD dissertation. Rensselaer Polytechnic Institute; 2004.
[55] Beaucage G. Journal of Applied Crystallography 1995;28:717–28.
[56] Beaucage G, Kammler HK, Pratsinis SE. Journal of Applied Crystallography 2004;37:523–35.
[57] Beaucage G. Journal of Applied Crystallography 1996;29:134–46.
[58] Schaefer DW, Rieker T, Agamalian M, Lin JS, Fischer D, Sukumaran S, et al. Journal of Applied Crystallography June 2000;33:587–91.
[59] Dobbins TA, Bruster EL, Oteri EU, Ilavsky J. Journal of Alloys and Compounds 2007;446:248–54.
[60] Roe R-J. Methods of X-ray and neutron scattering in polymer science. Oxford, UK: Oxford University Press; 2000.
[61] Higgins JS, Benoit HC. Polymers and neutron scattering. New York, USA: Oxford University Press; 1997.
[62] Schaefer DW, Beaucage G, Loy DA, Shea KJ, Lin JS. Chemistry of Materials 2004;16(8):1402–10.
[63] Schaefer DW, Zhao J, Dowty H, Alexander M, Orler EB. Soft Matter 2008;4(10):2071–9.
[64] Schaefer DW, Chen CY. Rubber Chemistry and Technology 2002;75(5):773–93.
[65] Schaefer DW, Justice RS. Macromolecules 2007;40(24):8501–17.
[66] Zhao C, Hu G, Justice R, Schaefer DW, Zhang S, Yang M, et al. Polymer 2005;46(14):5125–32.
[67] Justice RS, Wang DH, Tan LS, Schaefer DW. Journal of Applied Crystallography 2007;40:S88–92.
[68] Halpin JC, Kardos JL. Polymer Engineering and Science 1976;16(5):344–52.
[69] Hub C, Harton SE, Hunt MA, Fink R, Ade H. Journal of Polymer Science, Part B: Polymer Physics 2007;45(16):2270–6.
[70] Mondadori NML, Nunes RCR, Zattera AJ, Oliveira RVB, Canto LB. Journal of Applied Polymer Science 2008;109(5):3266–74.
[71] Tjong SC. Materials Science and Engineering R: Reports 2006;53(3–4):73–197.
[72] Fornes TD, Paul DR. Polymer 2003;44(17):4993–5013.
[73] Cannillo V, Bondioli F, Lusvarghi L, Montorsi M, Avella M, Errico ME, et al. Composites Science and Technology 2006;66(7–8):1030–7.
[74] Fukuda H, Kawata K. Fiber Science and Technology 1974;7(3):207–22.
[75] Smallwood HM. Journal of Applied Physics 1944;15:758–66.
[76] Jiang L, Zhang JW, Wolcott MP. Polymer 2007;48(26):7632–44.
[77] Ou YC, Yang F, Yu ZZ. Journal of Polymer Science, Part B: Polymer Physics 1998;36(5):789–95.
[78] Yang F, Ou YC, Yu ZZ. Journal of Applied Polymer Science 1998;69(2):355–61.
[79] Arrighi V, McEwen IJ, Qian H, Prieto MBS. Polymer 2003;44(20):6259–66.
[80] Liu FK, Hsieh SY, Ko FH, Chu TC. Colloids and Surfaces A: Physicochemical and Engineering Aspects 2003;231(1–3):31–8.
[81] Bafna A, Beaucage Mirabella F, Mehta S. 3D hierarchical orientation in polymer–clay nanocomposite films. Polymer 2003;44:1103–15.
[82] Ma D, Akpalu Y, Li Y, Siegel R, Schadler L. Journal of Polymer Science, Part B: Polymer Physics 2005;43(5):488–97.
[83] Sawyer WG, Freudenberg KD, Bhimaraj P, Schadler LS. A study on the friction and wear behavior of PTFE filled with alumina nanoparticles. Wear 2003;254:573–80.
[84] Schwartz CJ, Bahadur S. Studies on the tribological behavior and transfer film–counterface bond strength for polyphenylene sulfide filled with nanoscale alumina particles. Wear 2000;237:261–73.
[85] Ueki MM, Zanin M. Influence of additives on the dielectric strength of high-density polyethylene. IEEE Transactions on Dielectrics and Electrical Insulation 1999;6:876–81.
[86] Vaughan AS, Zhao Y, Barre LL, Sutton SJ, Swingler SG. On additives, morphological evolution and dielectric breakdown in low density polyethylene. European Polymer Journal 2003;39:355–65.
[87] Wang QH, Xu JF, Shen WC, Xue QJ. The effect of nanometer SiC filler on the tribological behavior of PEEK. Wear 1997;209:316–21.
[88] Wang QH, Xue QJ, Liu HW, Shen WC, Xu JF. The effect of particle size of nanometer ZrO_2 on the tribological behaviour of PEEK. Wear 1996;198:216–9.
[89] Yamano Y, Endoh H. Increase in breakdown strength of PE film by additives of azocompounds. IEEE Transactions on Dielectrics and Electrical Insulation 1998;5:270–5.

[90] Bureau MN, Denault J, Cole KC, Enright GD. The role of crystallinity and reinforcement in the mechanical behavior of polyamide-6/clay nanocomposites. Polymer Engineering and Science 2002;42:1897–906.
[91] Maiti P, Batt C, Giannelis E. New biodegradable polyhydroxybutyrate/layered silicate nanocomposites. Biomacromolecules 2007;8:3393–400.
[92] Petrovicova E, Knight R, Schadler LS, Twardowski TE. Journal of Applied Polymer Science 2000;78(13):2272–89.
[93] Priya L, Jog JP. Journal of Polymer Science, Part B: Polymer Physics 2002;40(15):1682–9.
[94] Saujanya C, Radhakrishnan S. Journal of Materials Science 2000;35(9):2319–23.
[95] Fornes TD, Paul DR. Polymer 2003;44(14):3945–61.
[96] Jimenez G, Ogata N, Kawai H, Ogihara T. Journal of Applied Polymer Science 1997;64(11):2211–20.
[97] Xie YC, Yu DM, Kong J, Fan XD, Qiao WQ. Journal of Applied Polymer Science 2006;100(5):4004–11.
[98] Zhang GS, Yan DY. Journal of Applied Polymer Science 2003;88(9):2181–8.
[99] Fornes TD, Yoon PJ, Keskkula H, Paul DR. Polymer 2001;42(25):9929–40.
[100] Fornes TD, Yoon PJ, Keskkula H, Paul DR. Polymer 2002;43(7):2121–2.
[101] Fornes TD, Yoon PJ, Hunter DL, Keskkula H, Paul DR. Polymer 2002;43(22):5915–33.
[102] Wunderlich B. Macromolecular physics. New York: Academic Press; 1973.
[103] Zuiderduin WCJ, Westzaan C, Huetink J, Gaymans RJ. Polymer 2003;44(1):261–75.
[104] Kim GM, Michler GH. Polymer 1998;39(23):5699–703.